ACS APPLIED MATERIALS & INTERFACES

www.acsami.org

Research Article

Orientational Disorder and Molecular Correlations in Hybrid Organic−Inorganic Perovskites: From Fundamental Insights to Technological Applications

Carlos Escorihuela-Sayalero, Ares Sanuy, Luis Carlos Pardo,* and Claudio Cazorla*

Cite This: ACS Appl. Mater. Interfaces 2025, 17, 1428−1440

Read Online

ABSTRACT: Hybrid organic−inorganic perovskites (HOIP) have emerged in recent years as highly promising semiconducting materials for a wide range of optoelectronic and energy applications. Nevertheless, the rotational dynamics of the organic components and many-molecule interdependencies, which may strongly impact the functional properties of HOIP, are not yet fully understood. In this study, we quantitatively analyze the orientational disorder and molecular correlations in archetypal perovskite $CH_3NH_3PbI_3$ (MAPI) by performing comprehensive molecular dynamics simulations and entropy calculations. We found that, in addition to the usual vibrational and orientational contributions, rigid molecular rotations around the C−N axis and correlations between neighboring molecules noticeably contribute to the entropy increment associated with the temperature-induced order−disorder phase transition, ΔS_t. Molecular conformational changes are equally infrequent in the low-T ordered and high-T disordered phases and have a null effect on ΔS_t. Conversely, the couplings between the angular and vibrational degrees of freedom are substantially reinforced in the high-T disordered phase and significantly counteract the phase-transition entropy increase resulting from other factors. Furthermore, the tendency for neighboring molecules to be orientationally ordered is markedly local, consequently inhibiting the formation of extensive polar nanodomains at both low and high temperatures. This theoretical investigation not only advances the fundamental knowledge of HOIP but also establishes physically insightful connections with contemporary technological applications like photovoltaics, solid-state cooling, and energy storage.

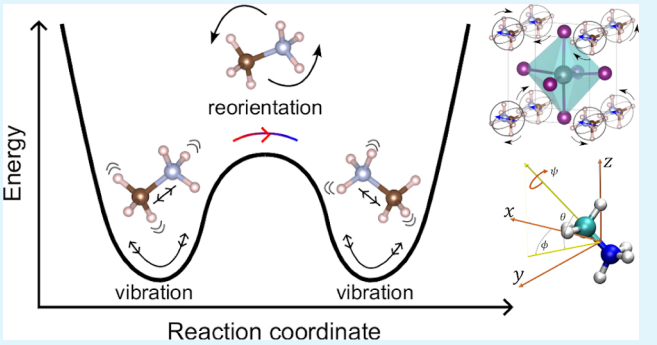

KEYWORDS: *hybrid organic−inorganic perovskites, molecular dynamics simulations, molecular rotational dynamics, molecular correlations, entropy calculations*

1. INTRODUCTION

Hybrid organic−inorganic perovskites (HOIP) are solids with the chemical formula ABX_3, where A and B−X represent organic and inorganic ions, respectively. Analogous to oxide perovskites, HOIP exhibits high-temperature crystalline phases with cubic symmetry. HOIP have emerged as a promising family of optoelectronic and energy materials, with significant potential for use in photovoltaic and light-emitting devices,[1−4] field-effect transistors,[5−7] energy storage,[8−10] and solid-state refrigerators,[11−14] among other technologies. Methylammonium lead iodide, $CH_3NH_3PbI_3$ (MAPI), is an archetypal HOIP that has been extensively investigated for solar cells and quantum dots applications.[15−19]

A characteristic physical trait of HOIP is that, upon increasing temperature, they undergo order−disorder phase transitions involving orientational molecular disorder, which on average gives rise to the high-symmetry cubic lattice.[20] Interestingly, the orientational dynamics of the organic cations may profoundly affect the functional properties and lattice dynamics of HOIP.[21−25] To cite few examples, the contribution of the molecular $CH_3NH_3^+$ (MA^+) rotations to the static dielectric response of MAPI has been estimated to be as large as ∼40%.[26] The origin of the hysteresis frequently observed in photocurrent−voltage measurements of MAPI-based solar devices, which offers promise for memristors and nonvolatile memory applications,[27] is also thought to be related to the rotational dynamics of molecular cations.[28] Additionally, the contribution of the orientational MA^+ degrees

Received: July 30, 2024
Revised: December 12, 2024
Accepted: December 16, 2024
Published: December 24, 2024

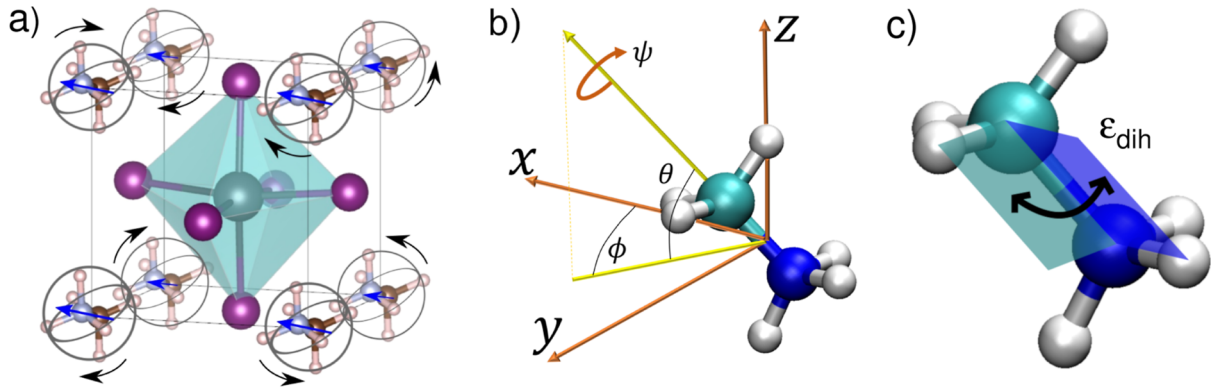

Figure 1. MAPI unit cell and MA molecule angular coordinates. (a) Sketch of MAPI in the high-temperature cubic perovskite phase. MA molecules are orientationally disordered. (b) Angles definition for describing the orientation of MA molecules. Angles θ and ϕ describe the orientation of the molecular C−N axis. Angle ψ refers to the rotation of the molecule around its C−N axis. (c) Dihedral angle describing the conformations of a MA molecule. Hydrogen, carbon, and nitrogen atoms are represented with white, green, and blue spheres, respectively.

of freedom to the caloric response of MAPI, as driven by external bias like hydrostatic pressure and electric field shifts, has been shown to be substantial.[29,30]

Despite these advancements, there remains a fundamental lack of understanding regarding the correlations between organic−organic and organic−inorganic ions, and how these correlations may impact the molecular orientational dynamics and, in turn, the functional properties of HOIP. For instance, it has been experimentally shown for MAPI that, even at temperatures well below the order−disorder phase transition point, the organic cations remain highly disordered and mobile.[31,32] Conversely, MA^+ reorientational motion is largely inhibited in mixed-halide hybrid perovskites such as $MAPbIBr_2$ and $MAPbI_2Br$.[33] The role of molecular correlations in the potential formation of ordered molecular domains also remains debatable.[26,28,34] Similarly, previous studies assessing the existence of caloric effects in HOIP have mostly considered organic cations as independent entities, thus neglecting the likely influence of many-molecule interdependencies on the observed solid-state cooling figures of merit.[11−14,30]

In this study, we delve into the analysis of molecular disorder and likely organic−organic and organic−inorganic ionic correlations in HOIP by conducting extensive molecular dynamics (MD) simulations for MAPI. Our quantitative investigations focus on evaluating the entropy change associated with the temperature-induced order−disorder phase transition occurring near room temperature (i.e., between the low-T tetragonal $I4/mcm$ and high-T cubic $Pm\bar{3}m$ phases[35,36]), ΔS_t, which is a physically interpretable and readily measurable quantity. We also address through MD simulations the question about the possible formation of ordered MA cation nanodomains at finite temperatures. Additionally, we establish physically insightful connections between our fundamental findings and technological applications of current interest like photovoltaics, solid-state cooling, and energy storage.

The organization of this article is as follows. First, we present a detailed description of the simulation approach employed for the evaluation of ΔS_t. Next, we report our computational results along with some discussions and subsequently provide a summary of the main conclusions. The technical details of our classical MD simulations and entropy calculation approach can be found in the Methods section.

2. COMPUTATIONAL APPROACH

2.1. MD Simulations. Classical MD simulations in the NpT ensemble (i.e., considering fixed number of particles, pressure, and temperature) have been conducted for bulk MAPI (Figure 1a) using the atomistic force field developed by Mattoni and collaborators.[37,38] This classical interatomic potential is based on a hybrid formulation of the Lennard−Jones and Buckingham pairwise interaction models and describes the MA molecules through harmonic-bonded interactions. Long-range electrostatic interactions are also appropriately accounted for by this atomistic force field. The high accuracy of this classical interatomic potential in providing correct MA^+ orientational configurations, as benchmarked by quantum first-principles simulations, has been previously demonstrated[30,39] (although it should be noted that it appreciably underestimates the temperature of the phase transition analyzed in this study, which involves the tetragonal $I4/mcm$ and cubic $Pm\bar{3}m$ phases of MAPI[30,35,36]). The technical details of our MD−NpT simulations can be found in the Methods section.

2.2. Reference Systems and Angles Definition. The orientation of each individual MA molecule has been determined in a fixed lab reference system through Euler angles θ_{lab}, ϕ_{lab}, and ψ_{lab} (Figure 1b). The angles θ_{lab} and ϕ_{lab} determine the orientation of each C−N molecular bond in the fixed reference frame. The angle ψ_{lab} describes the rotation of each molecule around its C−N molecular axis. In order to analyze possible molecular orientational correlations (see next sections), the relative orientations between MA molecules need to be tracked. For this end, a comobile reference system is set on an arbitrary molecule, and the orientation of the other molecules are referred to it through the angles θ_{rel}, ϕ_{rel} and ψ_{rel}. The origin of this comobile reference system is set at half the distance between the C−N atoms, with the z axis, pointing to the carbon atom, the y axis being perpendicular to the plane defined by the atoms N−C−H, and the x axis being perpendicular to the y and z axes. In addition, a dihedral angle, ε_{dih}, formed by the intersecting planes containing the H−C−N and C−N−H* atoms (where H belongs to the molecular methyl group and H* to the ammonia group, Figure 1c), is used to monitor possible MA^+ conformational changes.

2.3. Entropy Calculations. The entropy of the low-T ordered and high-T disordered phases of MAPI were

https://doi.org/10.1021/acsami.4c12762
ACS Appl. Mater. Interfaces 2025, 17, 1428−1440

determined as a function of temperature, S_{total}, using the relation

$$S_{total}(T) = S_{vib}(T) + S_{ang}(T) + S_{vib-ang}(T) \quad (1)$$

where S_{vib} is the entropy contribution resulting from the atomic vibrations, S_{ang} from the molecular angular degrees of freedom (i.e., orientational and conformational), and $S_{vib\text{-}ang}$ accounts for possible couplings between the vibrational and molecular angular degrees of freedom.

Likewise, the molecular angular entropy was assumed to be correctly evaluated with the expression

$$S_{ang}(T) = S_{ori}(T) + S_{conf}(T) + S_{ori-ori}(T) \quad (2)$$

where S_{ori} is the entropy contribution resulting from the orientational degrees of freedom of a single and noninteracting MA molecule, S_{conf} from the conformational changes of a single and noninteracting MA molecule, and $S_{ori\text{-}ori}$ accounts for possible orientational correlations between different molecules.

In this study, we primarily have focused on a comparative analysis of the entropy of the low-T ordered and high-T disordered phases of MAPI at the corresponding T-induced phase transition point (other possible external fields such as hydrostatic pressure and electric bias are set to zero). Thus, the physical quantity that is quantitatively analyzed in detail here corresponds to the phase-transition entropy change, defined as

$$\Delta S_t = \Delta S_{vib} + \Delta S_{ori} + \Delta S_{conf} + \Delta S_{ori-ori} + \Delta S_{vib-ang} \quad (3)$$

where $\Delta S_x \equiv S_x^{disord} - S_x^{ord}$ and all the entropy terms are evaluated at the phase-transition temperature T_t. The main improvement of this ΔS_t definition, compared to that in a previous work,[30] is the inclusion of molecular conformational changes (ΔS_{conf}), molecular orientational correlations ($\Delta S_{ori\text{-}ori}$), and possible couplings between the vibrational and molecular orientational degrees of freedom ($\Delta S_{vib\text{-}ang}$).

2.3.1. Vibrational Entropy. The vibrational density of states (VDOS) $\rho(\omega)$, where ω represents a lattice vibration frequency, provides information on the phonon spectrum of a crystal and allows the estimation of key thermodynamic quantities like the vibrational free energy, F_{vib}, and vibrational entropy, $S_{vib} \equiv -\frac{\partial F_{vib}}{\partial T}$. A possible manner of calculating $\rho(\omega)$ from the outputs of MD−NpT simulations consists in estimating the Fourier transform of the velocity autocorrelation function (VACF),[30,40,41] defined as

$$\mathrm{VACF}(t) = \langle \mathbf{v}(0)\cdot\mathbf{v}(t)\rangle = \frac{1}{N}\sum_i^N \mathbf{v}_i(0)\cdot\mathbf{v}_i(t) \quad (4)$$

where $\mathbf{v}_i(t)$ represents the velocity of the i-th particle and $\langle\cdots\rangle$ statistical average performed in the NpT ensemble. Subsequently, VDOS can be estimated as

$$\rho(\omega) = \int_0^\infty \mathrm{VACF}(t)e^{i\omega t}\mathrm{d}t \quad (5)$$

which fulfills the normalization condition

$$\int_0^\infty \rho(\omega)\mathrm{d}\omega = 3N \quad (6)$$

with $3N$ being the number of real and positively defined phonon frequency branches of the crystal.

Upon determination of ρ, the vibrational free energy can be straightforwardly estimated with the formula[42]

$$F_{vib}(T) = k_B T \times \int_0^\infty \ln\left[2\sinh\left(\frac{\hbar\omega}{2k_B T}\right)\right]\rho(\omega)\mathrm{d}\omega \quad (7)$$

where k_B is the Boltzmann's constant. Consistently, the vibrational entropy adopts the expression

$$S_{vib}(T) = -\int_0^\infty k_B \ln\left[2\sinh\left(\frac{\hbar\omega}{2k_B T}\right)\right]\rho(\omega)\mathrm{d}\omega + \int_0^\infty \frac{\hbar\omega}{2T}\tanh^{-1}\left(\frac{\hbar\omega}{2k_B T}\right)\rho(\omega)\mathrm{d}\omega \quad (8)$$

2.3.2. Molecular Orientational Entropy. For a continuous random variable x with probability density $f(x)$, its entropy is defined as:[43]

$$S = -\int_X f(x)\log f(x)\mathrm{d}x \quad (9)$$

where the integral runs over all possible values of x. If x represents a microstate characterizing a particular thermodynamic macrostate, then the following Gibbs entropy can be defined for the system of interest[44]

$$S_G = -k_B \int_X f(x)\log f(x)\mathrm{d}x \quad (10)$$

In an orientationally disordered crystal, molecules reorient in a quasi-random manner. By assuming the MA molecules in the HOIP crystal to be independent one from the other, one may estimate a probability density function for their orientation, $f(\theta_{lab}, \phi_{lab}, \psi_{lab})$, from the atomistic trajectories generated during long MD−NpT simulations. In this case, the following three-dimensional molecular orientational entropy can be defined, under the implicit assumption that the length of the MA molecules remains fixed[45−47]

$$S_{ori}(T) = S_0(T) - k_B \int f(\theta_{lab}, \phi_{lab}, \psi_{lab}) \log[f(\theta_{lab}, \phi_{lab}, \psi_{lab})] \times d\cos(\theta_{lab}) d\phi_{lab} d\psi_{lab} \quad (11)$$

where S_0 is a reference entropy term. (For a fluid, the value of this reference entropy term matches that of an ideal gas system under the same temperature and density conditions as the system of interest;[45−47] however, for an orientationally disordered solid, this reference term is not as straightforward to define).[30]

In practice, the calculation of S_{ori} entails the construction of histograms for which the continuous polar variables are discretized, $\{\theta_{lab}, \phi_{lab}, \psi_{lab}\} \rightarrow \{\theta_{lab,i}, \phi_{lab,i}, \psi_{lab,i}\}$. Accordingly, one may define the bin probabilities[43]

$$p_i(\theta_{lab,i}, \phi_{lab,i}, \psi_{lab,i}) \approx f(\theta_{lab,i}, \phi_{lab,i}, \psi_{lab,i}) \times \Delta\cos(\theta_{lab})\Delta\phi_{lab}\Delta\psi_{lab} \quad (12)$$

where $\Delta\cos(\theta_{lab})\,\Delta\phi_{lab}\,\Delta\psi_{lab}$ is the volume of a histogram bin (selected to be constant in this study). Consistently, one can rewrite the molecular orientational entropy in the discretized form

$$\Delta S_{ori}(T) = -k_B \sum_i p_i \log p_i + k_B \log[\Delta\cos(\theta_{lab})\Delta\phi_{lab}\Delta\psi_{lab}] \quad (13)$$

https://doi.org/10.1021/acsami.4c12762
ACS Appl. Mater. Interfaces 2025, 17, 1428−1440

where the value of the reference entropy term in eq 11 has been offset.

2.3.3. Molecular Conformational Entropy. At finite temperatures, MA molecules may undergo conformational changes that contribute to the total entropy, S_{conf}. The dihedral angle formed by the intersecting planes containing the H−C−N and C−N−H* atoms (where H belongs to the molecular methyl group and H* to the ammonia group, Figure 1c), ε_{dih}, may be used to monitor such conformational molecular changes. Analogously to the case of the orientational entropy, a probability density function can be estimated for this molecular dihedral angle from the atomistic trajectories generated during long MD−*NpT* simulations, $f(\varepsilon_{dih})$. Likewise, a bin probability can be defined, $p_i(\varepsilon_{dih,i}) \approx f(\varepsilon_{dih,i})\ \Delta\varepsilon_{dih}$, leading to the conformational entropy expression

$$\Delta S_{conf}(T) = -k_B \sum_i p_i \log p_i + k_B \log(\Delta\varepsilon_{dih}) \quad (14)$$

where $\Delta\varepsilon_{dih}$ is the fixed length of a histogram bin and the value of the corresponding reference entropy term has been offset.

2.3.4. Molecular Correlation Entropy. Equation 13 would provide the total orientational entropy for the MA molecules if these were completely independent of one from the other. However, neglecting molecular orientational correlations in HOIPs may lead to inaccuracies unless these correlations are rigorously quantified and demonstrated to be negligible. In this study, we account for the effects of molecular correlations in the entropy, $S_{ori\text{-}ori}$, by considering up to second-order terms in the many-body expansion of the full orientational entropy.[45−47] To this end, we monitor the relative orientation between pairs of molecules in a comobile reference system (Section 2.2) and calculate the molecular correlation entropy difference between the disordered and ordered phases like[45−47]

$$\Delta S_{ori-ori} = \frac{1}{2} k_B \sum_{i=1}^{n_{shell}} n_i \Delta S_{ori,i}^{rel} \quad (15)$$

where n_i is the number of molecules in the i-th spherical coordination shell (e.g., $n_1 = 6$ and $n_2 = 12$) and n_{shell} is the number of considered coordination shells (equal to 5 in the present study). The expression for the individual entropy terms $S_{ori,i}^{rel}$ is equivalent to that shown in eq 13, making the angular substitutions $\{\theta_{lab}, \phi_{lab}, \psi_{lab}\} \rightarrow \{\theta_{rel}, \phi_{rel}, \text{and } \psi_{rel}\}$.

It is worth noting that a simulation approach for the calculation of entropy terms, similar to the one introduced in this work, has been employed in two previous studies on the molecular crystals $LiCB_{11}H_{12}$[48] and $C_5H_{12}O_2$.[49] In both cases, we observed consistently good agreement for the total phase-transition entropy change when compared to results obtained using alternative thermodynamic approaches, such as the Clausius−Clapeyron (CC) equation and direct calculation of the internal energy difference from MD−*NpT* simulations (see Section 3.6 for further details of these methods). Thus, despite the limitations in performing additional benchmark calculations to further validate the accuracy of our entropy estimates for MAPI (e.g., harmonic and thermodynamic integration approaches[50−52]), due to its highly anharmonic and orientationally disordered nature, we are confident in the reliability and numerical precision of our simulation study.

3. RESULTS AND DISCUSSION

In a previous work,[30] we already estimated the phase-transition entropy change for MAPI associated with the temperature-induced order−disorder phase transition occurring near room temperature (i.e., between the low-T tetragonal $I4/mcm$ and high-T cubic $Pm\bar{3}m$ phases[35,36]) through MD−*NpT* simulations by considering vibrational and molecular orientational degrees of freedom. Nevertheless, in this study, we present several critical improvements to our original ΔS_t calculation, which can be generalized to other HOIPs and solids exhibiting molecular orientational disorder (e.g., plastic crystals[48,53−56]). These critical computational improvements include considering entropy contributions from molecular conformational changes (ΔS_{conf}), molecular orientational correlations ($\Delta S_{ori\text{-}ori}$), and possible couplings between the vibrational and molecular orientational degrees of freedom ($\Delta S_{vib\text{-}ang}$) (Section 2.3). Next, we present and discuss the calculation of ΔS_t term-by-term, comment on the potential formation of ordered MA^+ nanodomains, and make insightful connections with technological applications. Our main entropy numerical findings are summarized in Table 1.

Table 1. Contributions to the Total Entropy Change Associated with the *T*-Induced Order−Disorder Phase Transition in MAPI, ΔS_t[a]

	ΔS_{vib}	ΔS_{ori}	ΔS_{conf}	$\Delta S_{ori\text{-}ori}$	$\Delta S_{vib\text{-}ang}$	ΔS_t
(J K^{-1} kg^{-1})	+21.7	+13.5	≈0	+3.8	−12.6	+26.4
(%)	+82	+51	≈0	+15	−48	+100

[a] $\Delta S_x \equiv S_x^{disord} - S_x^{ord}$ and all the entropy terms are evaluated at the phase-transition temperature, T_t. ΔS_{vib} represents contributions from the lattice vibrations, ΔS_{ori} from the MA orientational degrees of freedom, ΔS_{conf} from the MA conformations, $\Delta S_{ori\text{-}ori}$ from the molecule−molecule orientational correlations, and $\Delta S_{vib\text{-}ang}$ from the couplings between the vibrational and molecular angular degrees of freedom.

3.1. Vibrational Entropy. The simulation results presented in this section have been mostly reported in a previous work of ours.[30] These previous numerical findings are reproduced here for coherence and completeness reasons.

Figure 2 shows the VDOS and partial organic and inorganic contributions estimated for MAPI at temperatures slightly above and below the simulated order−disorder phase transition points (i.e., 245 and 240 K). The VDOS contribution corresponding to the inorganic part, namely, the PbI_3 octahedra, is clearly dominant in the low-frequency range of $0 \leq \nu \leq 5$ THz (Figure 2a−b). This result follows from the fact that the lighter atoms, which typically vibrate at higher frequencies, entirely reside in the organic molecules. Consistently, the range of moderate and high frequencies, $\nu \geq 5$ THz, is mostly governed by MA cation vibrations.

Albeit the VDOS enclosed in Figure 2a−b may seem quite similar at first glance, there are significant differences among them (Figure 3a). In particular, the high-T disordered phase accumulates more phonon modes in the low-frequency range $0 \leq \nu \leq 2$ THz than does the low-T ordered phase. This effect has a strong influence on the vibrational entropy of the system, S_{vib}, which is significantly larger for the high-T disordered phase. It is worth noting that in previous first-principles computational studies,[57,58] the low-frequency vibrations of the PbI_3 octahedra (Figure 3b) were associated with bending and stretching modes, while the low-frequency phonon modes of the MA cations were linked to a combination of libration and translation (Figure 3c).

https://doi.org/10.1021/acsami.4c12762
ACS Appl. Mater. Interfaces 2025, 17, 1428−1440

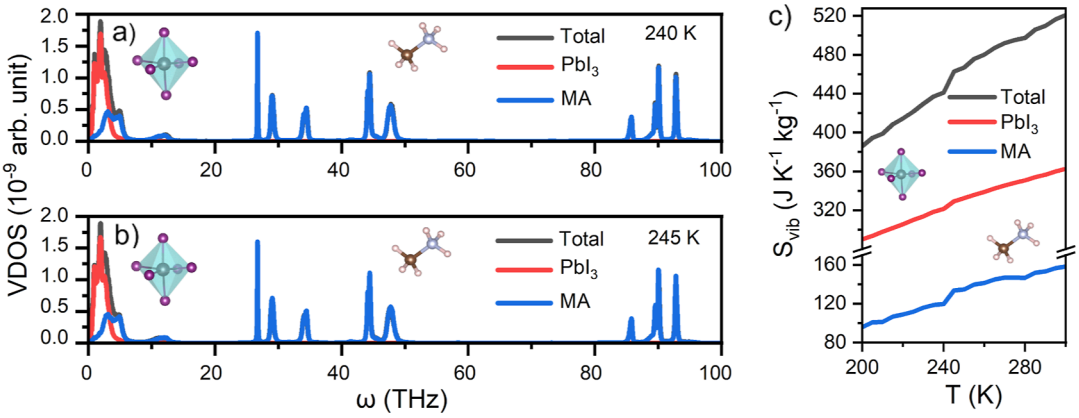

Figure 2. VDOS and vibrational entropy (S_{vib}) of MAPI calculated at different temperatures. VDOS results were obtained (a) for the ordered phase at T = 240 K and (b) for the disordered phase at T = 245 K. (c) Vibrational entropy of MAPI expressed as a function of temperature.

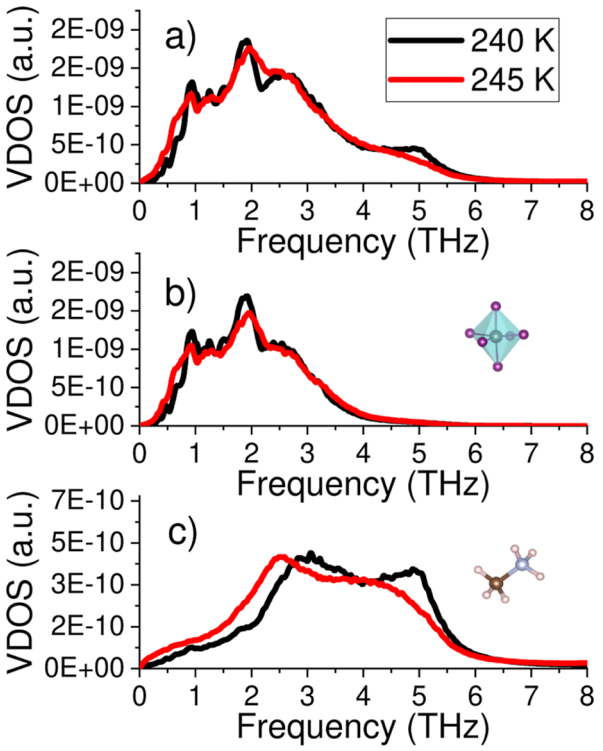

Figure 3. VDOS of MAPI in the low-frequency range. (a) Total VDOS for the ordered phase at T = 240 K and disordered phase at T = 245 K. (b) Inorganic contribution to the total VDOS for the ordered phase at T = 240 K and disordered phase at T = 245 K. (c) Organic contribution to the total VDOS for the ordered phase at T = 240 K and disordered phase at T = 245 K. To improve the visualization, a change of scale has been applied on the coordinate axis of this figure.

Figure 2c shows the S_{vib} values estimated as a function of temperature. A clear surge in vibrational entropy is observed at the phase-transition point, ΔS_{vib} = +21.7 J K^{-1} kg^{-1}. The positive sign indicates that the vibrational entropy of the high-T disordered phase is larger than that of the low-T ordered phase. The primary contribution to this vibrational entropy increase comes from the molecular cations, which is equal to +13.9 J K^{-1} kg^{-1} and almost twice as large as that calculated for the inorganic part (namely, +7.8 J K^{-1} kg^{-1}). Thus, although the low-frequency range in VDOS is dominated by the inorganic anions, the organic MA cations have a larger influence on the vibrational entropy change associated with the order−disorder phase transition, ΔS_{vib}.

3.2. Molecular Orientational Entropy. To estimate the orientational entropy associated with the order−disorder phase transition of MAPI, ΔS_{ori}, we have extended the computational approach introduced in a previous work of ours[30] to include the three Euler angles that fully determine the orientation of an arbitrary (and rigid) MA cation, namely, $\{\theta, \phi, \psi\}$ (Figure 1b). To calculate ΔS_{ori}, we initially assumed the MA cations to be independent of each other. Consequently, the three Euler molecular angles should be referred to the stationary lab reference system, namely, $\{\theta_{lab}, \phi_{lab}$, and $\psi_{lab}\}$ (Section 2.2). The complete molecular orientation maps thus correspond to three-dimensional probability density functions (pdf) considering those three angles.

In the previous work,[30] the ψ_{lab} angle, which accounts for the rotation of the MA molecules around their C−N molecular axis (Figure 1b), was not considered, thus potential entropy contributions resulting from this angular degree of freedom were totally neglected. Results for the full MA orientational pdf calculated for the low-T ordered and high-T disordered phases of MAPI, as projected onto two different planes, are shown in Figures 4a and 5a, respectively.

As shown in Figure 4a, in the low-T ordered phase, the MA cations do not reorient since the equilibrium molecular orientations, represented by bright spots in the $\cos(\theta_{lab})-\phi_{lab}$ pdf, are disconnected (i.e., angular transition paths connecting them are absent). This outcome was anticipated and is consistent with our previous results.[30] On the other hand, as expected, in the high-T disordered phase, the molecular C−N axis are free to reorient, as indicated by the regions of nonzero probability appearing between the equilibrium molecular orientations (Figure 5a). For this phase, and also in agreement with our previous findings,[30] there a six possible equilibrium molecular orientations: two "apical" [$\cos(\theta_{lab}) = \pm 1$, $\phi_{lab} = 0$] and four "equatorial" [$\cos(\theta_{lab}) = 0$, $\phi_{lab} = \pm 60, 120°$].

Figures 4a and 5a also show the pdf associated with the azimuthal angle ψ_{lab}, which describes the rigid rotation of the MA cations around their C−N axis (Figure 1b). Interestingly and surprisingly, it is found that for both the low-T ordered and high-T disordered phases of MAPI, there are rotational paths connecting high probability regions (i.e., equilibrium molecular orientations). This result implies that close to the transition temperature the molecules rotate around their C−N axis in both the ordered and disordered states. It is worth

https://doi.org/10.1021/acsami.4c12762
ACS Appl. Mater. Interfaces 2025, 17, 1428−1440

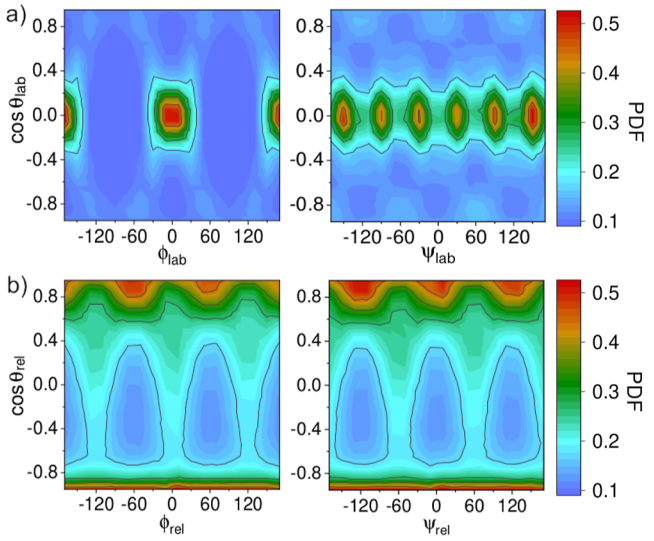

Figure 4. Bivariate angular probability density function (pdf) for MA molecules in the low-T ordered phase. Results were obtained at T = 240 K in the (a) lab-fixed ("lab") and (b) molecule-mobile ("rel") reference systems. For the "rel" case, the six MA cations within the first coordination shell were considered. Red, green, and blue colors represent high-probability, medium-probability, and low-probability configurations, respectively.

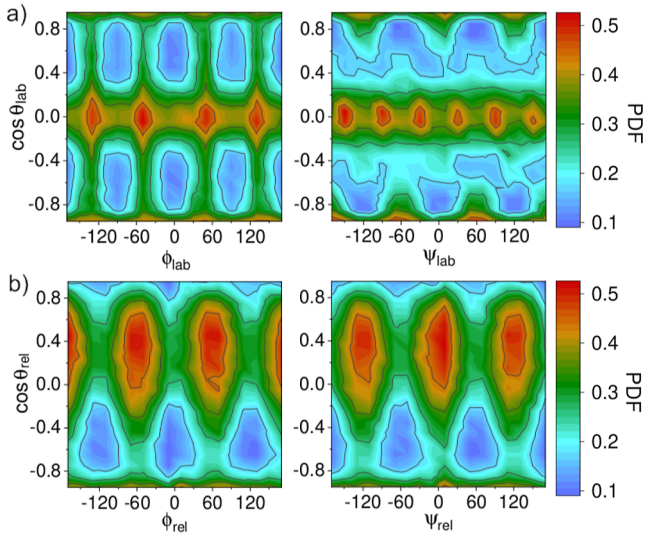

Figure 5. Bivariate angular probability density function (pdf) for MA molecules in the high-T disordered phase. Results were obtained at T = 260 K in the (a) lab-fixed ("lab") and (b) molecule-mobile ("rel") reference systems. For the "rel" case, the six MA cations within the first coordination shell were considered. Red, green, and blue colors represent high-probability, medium-probability, and low-probability configurations, respectively.

noting that this type of azimuthal orientational disorder does not break the symmetry of the crystal (i.e., the corresponding equilibrium configurations are equivalent among them) and hence cannot be resolved in diffraction experiments.[59−62] This class of molecular disorder, present in both the low-T ordered and high-T disordered phases of MAPI, is consistent with previous results reported in experimental neutron scattering works.[22,63] Nevertheless, in our simulation study, in contrast to experiments, we are able to clearly distinguish between rotations of the MA molecule as a whole around the C−N axis and conformational molecular changes involving independent rotations of either the ammonia or methyl group (see next section).

The orientational phase-transition entropy change obtained from the two-dimensional pdf associated with the two angles $\{\cos(\theta_{lab}), \phi_{lab}\}$ amounts to +10.7 J K^{-1} kg^{-1}.[30] However, when considering the full orientational pdf associated with the three Euler angles $\{\cos(\theta_{lab}), \phi_{lab}$, and $\psi_{lab}\}$, it is found that ΔS_{ori} = +13.5 J K^{-1} kg^{-1}. Therefore, by including the molecular azimuthal degree of freedom, the orientational entropy change increases by approximately 25%, thus representing a substantial correction. It is noted in passing that the degree of disorder associated with the molecular azimuthal angle ψ_{lab} is larger for the high-T phase.

It is instructive to compare the ΔS_{ori} value obtained from the atomistic MD−NpT simulations with that estimated straightforwardly from symmetry and simplified thermodynamic arguments. From the $\cos(\theta_{lab})-\phi_{lab}$ pdf shown in Figures 4a and 5a, it is observed that the MA cations can adopt two possible orientations in the low-T ordered phase and six in the high-T disordered phase. This elementary counting leads to a rough orientational entropy change of k_B(ln6-ln2), which equals 14.7 J K^{-1} kg^{-1} and is approximately 40% larger than the correct ΔS_{ori} value obtained directly from the atomistic simulations. We may thus conclude that such a rough estimation of the orientational entropy change, although it appears to be a reasonable initial guess, is quantitatively not accurate.

3.3. Molecular Conformational Entropy. In the previous section, we asserted that in both the low-T ordered and high-T disordered phases of MAPI, the MA cations perform rigid rotations around their molecular C−N axis, which do not affect the symmetry of the crystalline lattice. However, changes in the azimuthal angle ψ_{lab} could, in principle, also be due to conformational changes of the MA cation associated with disconnected rotations of the methyl (CH_3) and/or ammonia (NH_3) groups at the ends of the molecule. To check this possibility, we plot in Figure 6 and 7 the time evolution of the molecular angles $\{\psi_{lab}, \varepsilon_{dih}\}$ for the low-T ordered and high-T disordered phases, respectively, where ε_{dih} is the dihedral angle formed by the intersecting planes containing the H−C−N and C−N−H* atoms (H belonging to the molecular methyl group and H* to the ammonia group, Figure 1c). For the sake of completeness, we also represent the dynamical evolution of the angles θ_{lab} and ϕ_{lab} for the high-T disordered phase in Figure 7.

For the low-T ordered phase (Figure 6), it is clearly observed that the sequence of ψ_{lab} and ε_{dih} changes occurring over time are uncorrelated. For instance, the dihedral angle changes twice its value within the time interval of 80 ps, from −60 to +60° and vice versa (Figure 6b), while the azimuthal angle changes several tens of times its value, $-180° \leq \psi_{lab} \leq +180°$, within the same time interval (Figure 6a). A very similar behavior is also appreciated for the high-T disordered phase (Figure 7a,d). Consequently, it can be safely concluded that owing to the absence of time correlations between the angles ψ_{lab} and ε_{dih} in both phases, changes in the azimuthal angle correspond to rigid molecular rotations around the C−N axis. We note in passing that the dynamics of the dihedral angle is extremely slow in both the low-T ordered and high-T disordered phases, which denotes the high rigidity of the MA^+ molecules.

https://doi.org/10.1021/acsami.4c12762
ACS Appl. Mater. Interfaces 2025, 17, 1428−1440

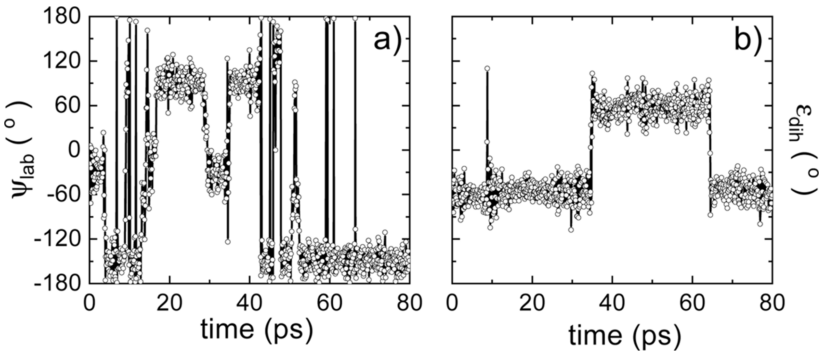

Figure 6. Dynamical description of the MA cation orientation around its C−N axis and molecular conformations for the low-temperature ordered phase. Time evolution of (a) the azimuthal angle ψ_{lab} describing the MA^+ rotation around its C−N axis and (b) the dihedral angle ε_{dih} describing molecular conformation (Figure 1).

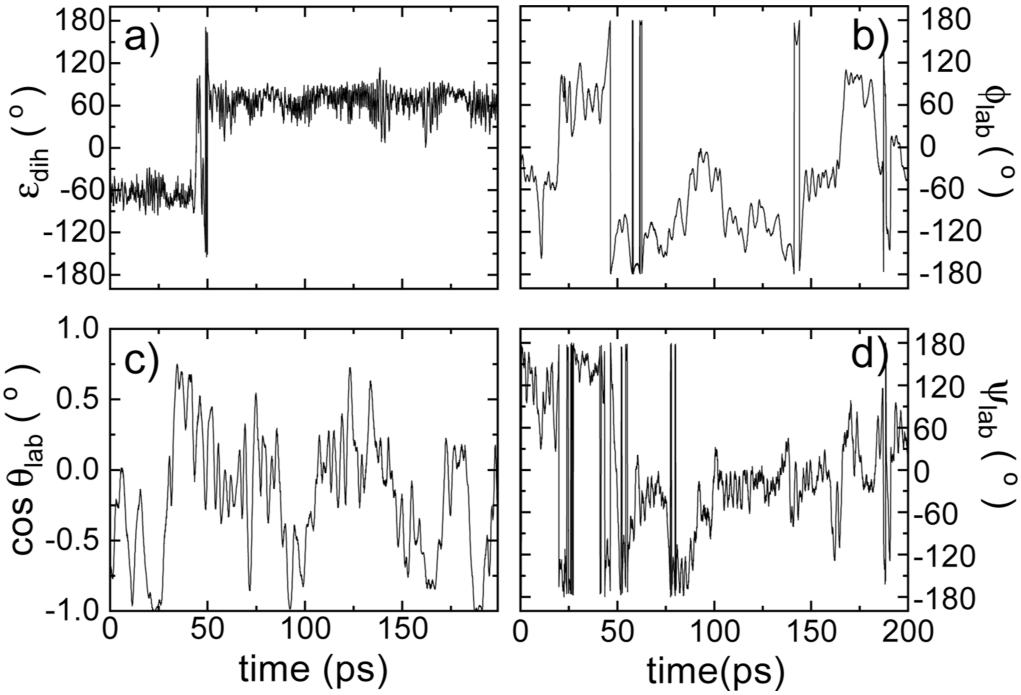

Figure 7. Dynamical description of the MA cation orientation around its C−N axis and molecular conformations for the high-temperature disordered phase. Time evolution of (a) the dihedral angle ε_{dih} describing molecular conformation, and the rest of MA angles (b) ϕ_{lab}, (c) θ_{lab}, and (d) ψ_{lab} describing molecular orientation (Figure 1).

Figure 8 shows the pdf estimated for the molecular dihedral angle ε_{dih} for both the low-T ordered and high-T disordered phases of MAPI, close to the phase-transition temperature. It is observed that ε_{dih} essentially adopts equilibrium values ±60 and ±180° in both phases. Additionally, the estimated pdf are very similar for the two phases. As a consequence, the phase-transition entropy variation associated with molecular conformational changes (eq 14) turns out to be practically null for MAPI, namely, $\Delta S_{conf} \approx 0$. It can be concluded then that the MA cation presents high rigidity in both the low-T ordered and high-T disordered phases and that below and close to room temperature molecular conformational disorder in MAPI is strongly inhibited.

3.4. Molecular Correlation Entropy. Figures 4b and 5b show the pdf estimated for the three Euler angles $\{\theta_{rel}, \phi_{rel}, \psi_{rel}\}$ describing the relative orientation between closest MA cations (i.e., within the first coordination shell) in a comobile molecular reference system (Section 2.2) for the low-T ordered and high-T disordered phases of MAPI, respectively. Using these orientational probability maps and others involving successive coordination shells, it is possible to quantify molecular ordering and the phase-transition entropy change associated with the molecule−molecule correlations, as explained in Section 2.3.4.

In the low-T ordered phase (Figure 4b), the relative orientation between the closest molecules is most likely for $\cos(\theta_{rel}) = \pm 1$, which translates into parallel and antiparallel C−N bond arrangements or, equivalently, parallel and antiparallel molecular dipoles. Interestingly, it is observed that these maximum probability regions differ in shape. The reason for this asymmetry is the following. Two out of the six closest MA cations are parallel $[\cos(\theta_{rel}) = +1]$, located in the "tail" and "head" positions of the central MA^+, and four are antiparallel $[\cos(\theta_{rel}) = -1]$, positioned in the equatorial plane of the central MA^+. The molecules parallel to the reference MA cation slightly tilt their C−N axis relative to the central one, to

https://doi.org/10.1021/acsami.4c12762
ACS Appl. Mater. Interfaces 2025, 17, 1428−1440

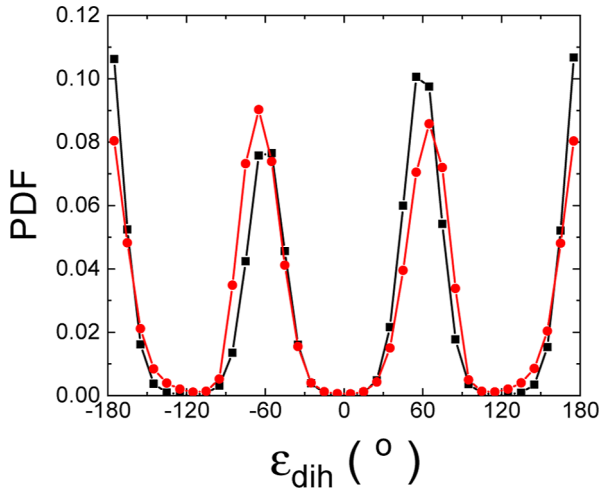

Figure 8. Angular probability density function (pdf) for the molecular dihedral angle ε_{dih} describing the conformation of MA molecules. Results are represented for the low-T ordered (red circles) and high-T disordered (black squares) phases. Solid lines are guides to the eye.

change their ψ_{rel} orientation, causing $\cos(\theta_{rel})$ to slightly depart from +1. This behavior, however, is not observed for the antiparallel molecules.

In the high-T disordered phase (Figure 5b), strong orientational correlations between the closest MA molecules are evident, as otherwise much more uniform and symmetric probability maps would have been obtained. For example, molecular parallel arrangements are strongly suppressed at high temperatures, as shown by the very low probability estimated for $\cos(\theta_{rel}) = +1$. In this case, the most likely relative MA^+ orientations correspond to three different molecular arrangements resulting in $\cos(\theta_{rel}) \approx 0.4$, which compensates for the total dipole moment deriving from the also highly probable antiparallel configuration $[\cos(\theta_{rel}) = -1]$. It is worth noting that the number of equilibrium relative orientations is the same for the low-T ordered and high-T disordered phases, totaling four. The most significant molecular orientation difference between the two phases is a shift in the maximum probability from $\theta_{rel} \approx 0°$ at low temperatures to $\theta_{rel} \approx 66°$ at high temperatures.

In view of the fact that the reorientational MA^+ motion in MAPI is correlated, we calculated the entropy difference between the low-T ordered and high-T disordered phases resulting from the molecular correlations at the corresponding phase-transition temperature, $\Delta S_{ori\text{-}ori}$ (Section 2.3.4). A positive (negative) $\Delta S_{ori\text{-}ori}$ value would indicate larger (smaller) molecular correlation entropy in the high-T disordered phase and consequently less (more) correlated molecular orientational dynamics in that phase. Adding consecutive entropy terms up to the fifth coordination shell (i.e., a maximum radial distance of 14.7 Å and 56 molecules), we estimated $\Delta S_{ori\text{-}ori} = +3.8$ J K^{-1} kg^{-1}. It was found that this molecular correlation entropy was already numerically converged to within 0.1 J K^{-1} kg^{-1} at the fourth coordination shell, which involves a maximum radial distance of 13.2 Å and 32 molecules. The calculated $\Delta S_{ori\text{-}ori}$ value is positive, suggesting more substantial correlations in the molecular orientational dynamics of the low-T phase. Moreover, $\Delta S_{ori\text{-}ori}$ is comparable in magnitude, for instance, to the phase-transition entropy gain associated with the azimuthal angle ψ_{lab} (Section 3.2) and hence is not negligible.

3.5. Molecular Dipoles Ordering. To further elucidate the molecular orientational disorder in MAPI and evaluate the possible formation of ordered MA^+ nanodomains at finite temperatures, we represent in Figure 9 the pdf estimated for

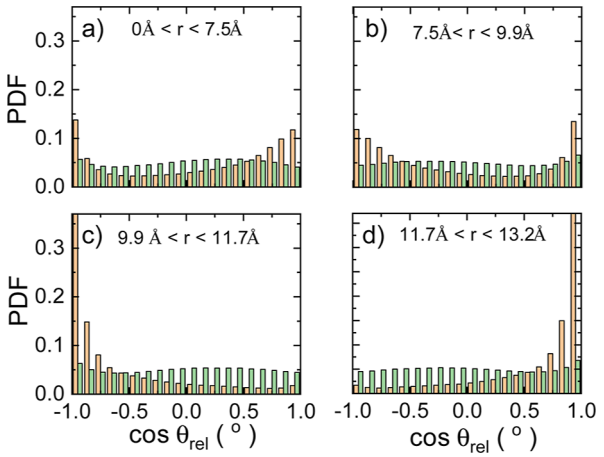

Figure 9. Probability density function (pdf) for the molecular dipole orientation in the coMobile ("rel") reference system obtained across successive coordination shells. Results obtained for (a) first, (b) second, (c) third, and (d) fourth coordination shells. Orange and green bars represent results obtained for the low-temperature ordered and high-temperature disordered phases, respectively.

the angular quantity $\cos(\theta_{rel})$ across successive coordination shells (i.e., from the first up to the fourth). Although our primary focus is on the molecular structure of the high-T disordered phase, we have also included pdf results for the low-T ordered phase in Figure 9 to facilitate the interpretation and comparison of our findings.

It is clear from Figure 9 that the relative orientation between molecules in the high-T disordered phase follows a fairly uniform probability distribution within all of the analyzed coordination shells, implying that there is no particularly preferred MA^+ orientation. For instance, the average value of the angular pdf within the first coordination shell (Figure 9a) amounts to $\langle \cos(\theta_{rel}) \rangle = 0.02$, with similar values obtained for the other consecutive coordination shells. Conversely, the pdf of the low-T ordered phase exhibits well-defined peaks within all of the coordination shells at $\cos(\theta_{rel}) = \pm 1$, as expected (Section 3.4), leading to general antipolar ordering.

Interestingly, a very subtle alternation from marginally parallel to marginally antiparallel relative molecular arrangements is observed for the high-T disordered phase as the radial distance increases. However, this slight variation of relative MA^+ orientations developing through successive coordination shells does not induce the appearance of nanoregions with well-defined polarization. This outcome is illustrated in Figure 10, where we compare the pdf estimated for the number of parallel and antiparallel MA cations to a chosen one within the first coordination shell, as directly obtained from our MD–NpT simulations, and consider completely random, and thus uncorrelated, relative molecular orientations. No appreciable differences are observed between the two pdfs. It can then be concluded that the appearance of polar nanodomains in MAPI is precluded since the MA molecules tend to orient homogeneously throughout the crystal. A similar behavior has been recently reported for a plastic crystal.[64]

https://doi.org/10.1021/acsami.4c12762
ACS Appl. Mater. Interfaces 2025, 17, 1428–1440

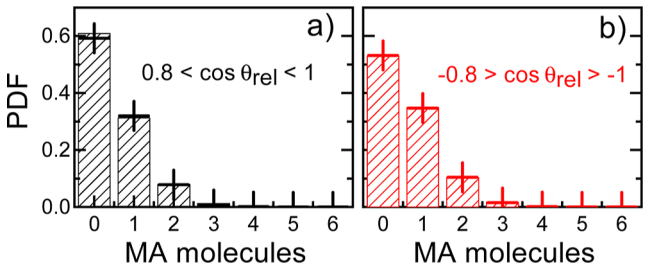

Figure 10. Probability distribution function (pdf) for the number of molecules in the first coordination shell of a MA cation that are parallel and antiparallel to it. Results were obtained by averaging over all molecules and simulation time. Pdf corresponding to (a) parallel and (b) antiparallel relative molecular dipole orientations (black and red boxes). The crosses in the figures represent analogous results obtained for a random distribution of relative molecular dipole orientations.

3.6. Vibrational−orientational Correlation Entropy.

There is an additional source of potential entropy variation in MAPI related to the correlations between the molecular angular and vibrational degrees of freedom, $\Delta S_{\text{vib-ang}}$ [eq 3], which mainly results from the interdependencies between the organic and inorganic ions. Unlike the rest of the terms in eq 3, there is neither an analytical expression nor a computational recipe to directly evaluate $\Delta S_{\text{vib-ang}}$. Nevertheless, this particular entropy variation can be indirectly estimated at the order−disorder phase-transition point using simple thermodynamic arguments and MD−*NpT* simulations, as we explain below.

At the order−disorder phase-transition temperature, the Gibbs free energy ($G \equiv H - TS$, where H stands for enthalpy) of the low-T ordered and high-T disordered phases of MAPI should be equal. Therefore, it follows that $\Delta S_t = \Delta H_t / T_t$. Since our MD−*NpT* simulations are performed at zero pressure, the enthalpy difference between the high-T disordered and low-T ordered phases are equal to their internal energy difference at the phase-transition temperature, namely, $\Delta H_t = \Delta U_t$. This latter quantity can be directly obtained with great precision from the MD−*NpT* simulations and, consequently, ΔS_t as well. Knowing the value of all the entropy terms in eq 3 except $\Delta S_{\text{vib-ang}}$, it follows that

$$\Delta S_{\text{vib-ang}} = \Delta S_t - \Delta S_{\text{vib}} - \Delta S_{\text{ori}} - \Delta S_{\text{conf}} - \Delta S_{\text{ori-ori}} \quad (16)$$

From our MD−*NpT* atomistic simulations, we obtained ΔS_t = +26.4 J K^{-1} kg^{-1} for the T-induced order−disorder phase transition occurring in MAPI. This value is in fairly good agreement with an equivalent estimation reported in work,[30] ΔS_t^{CC} = +28.4 J K^{-1} kg^{-1}, which was based on the Clausius−Clapeyron (CC) method and is therefore more prone to numerical errors. Using eq 16 and the phase-transition entropy change values reported in previous sections, we conclude that $\Delta S_{\text{vib-ang}}$ = −12.6 J K^{-1} kg^{-1} (Table 1). The size of this vibrational−orientational correlation entropy is roughly 50% of the total phase-transition entropy change, which is surprisingly large and comparable in absolute value to the entropy change contribution ΔS_{ori} resulting from the individual MA$^+$ orientational degrees of freedom (Section 3.2). This source of entropy change in MAPI, and arguably in HOIP in general, has not been considered in previous studies but, given its large magnitude, should not be neglected.

Interestingly, the sign of the estimated $\Delta S_{\text{vib-ang}}$ is negative, unlike the rest of the entropy terms in eq 3. Consequently, the crossed vibrational−orientational contribution decreases the total phase-transition entropy change. From a physical point of view, the negative sign of $\Delta S_{\text{vib-ang}}$ can be understood in terms of the couplings between the vibrational and molecular angular degrees of freedom, which are substantially reinforced in the high-T disordered phase (i.e., a smaller entropy is identified here with a higher degree of concertation). This reasoning is consistent with the large increase in vibrational entropy observed across the order−disorder phase transition (Section 3.1). In particular, correlations extending over a large number of atoms, both organic and inorganic, may lead to low-frequency phonon modes due to the large effective mass associated with such lattice vibrations (recall that for harmonic oscillations, $\omega \propto m^{-1/2}$).[48] Additionally, the overlap between the PbI_3 and CH_3NH_3 lattice excitations also increases in the disordered phase, particularly in the limit of very low frequencies (Figure 3), thus suggesting a larger degree of organic−inorganic concertation in the high-T phase.

3.7. Connections to Technological Applications.

Table 1 reports the value of the different contributions to the total entropy change associated with the T-induced order−disorder phase transition occurring in MAPI, as well as their relative percentage. The three entropy variations ΔS_{vib}, ΔS_{ori}, and $\Delta S_{\text{vib-ang}}$ are found to be the largest in absolute value and similar in size, with the peculiarity that only the sign of the crossed vibrational−orientational entropy change is negative. In what follows, we make connections between our atomistic simulation findings and a few technological applications in which HOIPs are used or have been proposed as promising, namely, solid-state cooling, photovoltaics, and energy storage.

Solid-state cooling is an energy efficient and ecologically friendly technique with potential for solving the environmental problems posed by conventional refrigeration technologies relying on compression cycles of greenhouse gases.[65−67] Upon moderate magnetic, electric, or mechanical field variations, auspicious caloric materials experience large adiabatic temperature variations ($|\Delta T| \sim 1-10$ K) due to phase transformations entailing large isothermal entropy changes ($|\Delta S| \sim$ 10−100 J K^{-1} kg^{-1}). HOIP have shown great promise as caloric materials because their order−disorder phase transition can be driven near room temperature under the influence of various external bias like hydrostatic pressure and electric fields.[11−14,29,30,34,68]

However, the entropy changes associated with the order−disorder phase transition in HOIP ($|\Delta S| \sim$ 10 J K^{-1} kg^{-1}) are about an order of magnitude smaller than those measured in plastic crystals ($|\Delta S| \sim$ 100 J K^{-1} kg^{-1}), a related family of materials composed exclusively of organic molecules. Plastic crystals like neopentilglycol ($C_5H_{12}O_2$) have recently revolutionized the field of solid-state refrigeration due to the huge latent heat associated with their molecular order−disorder phase transition (similar to that of MAPI), easy synthesis, low toxicity, and reduced economic cost.[48,53−56] The physical reason for the difference in phase-transition entropy change between HOIP and plastic crystals may partly originate from the $\Delta S_{\text{vib-ang}}$ contributions in the former materials, which, as revealed in this study, tend to reduce ΔS_t. Consequently, a potential rational design strategy to improve the caloric figures of merit of HOIP could be to minimize the crossed vibrational−orientational couplings through chemical and/or structural engineering.[69]

In solar cells, the dielectric function of the light-absorbing materials, ε, is of the upmost importance as it directly impacts

https://doi.org/10.1021/acsami.4c12762
ACS Appl. Mater. Interfaces 2025, 17, 1428−1440

the binding energy of excitons, E_{bind} (i.e., photogenerated electron−hole pairs that remain electrostatically bound). In particular, E_{bind} should be minimized to facilitate the dissociation of excitons into free charge carriers and prevent electron−hole recombination.[70] According to the Wannier-Mott model $E_{bind} \propto 1/\varepsilon^2$,[71] meaning larger (smaller) values of ε correspond to smaller (larger) exciton binding energies. In HOIP, lattice vibrations are intrinsically coupled with cation orientational motion, both of which are considered to influence the material's optoelectronic performance.[21−26,28] Phonons can significantly modulate the band gap, charge transport, and exciton dynamics.[72,73] Cation orientational dynamics may affect properties such as ferroelectricity, ion transport, and the dielectric behavior of HOIP.[74−76]

In the specific case of MAPI, ε is strongly influenced by the phonons and molecular cation rotations, which both contribute to the lattice component of the dielectric constant in the high-T disordered phase,[77−79] increasing it from 5 to 33.[26,80,81] As a result, the excitonic binding energy of MAPI decreases from approximately 16 meV in the low-T ordered phase to 6 meV in the high-T disordered phase.[26,81]

In this study, we have theoretically demonstrated that the couplings between phonons and cation orientational dynamics in MAPI are substantial and crucial for evaluating the entropy change associated with their T-induced order−disorder phase transition. Furthermore, by calculating the entropy difference term $\Delta S_{vib\text{-}ang}$, we have determined that vibrational−orientational couplings are stronger in the high-T disordered phase compared to those in the low-T ordered phase. This enhancement of the molecular cation−ionic anion interactions in the orientationally disordered phase may partially explain the observed increase in ε and the corresponding decrease in E_{bind}. Consequently, a potential rational design strategy to reduce exciton binding energy in light-absorbing HOIPs, thereby mitigating detrimental electron−hole recombinations, could involve enhancing their vibrational−orientational couplings, either through chemical modifications and/or nanostructuring.[69] A possible descriptor for quantifying the degree of interplay between organic cation orientation and octahedral anion vibration in the high-T disordered phases of HOIPs, could be the overlap between low-frequency lattice phonons with prevalent molecular and ionic character.[52]

Energy storage materials are crucial for powering vehicles, buildings, and portable devices in the push for clean energy. Lithium-ion batteries dominate the market, offering high energy density, low self-discharge, a negligible memory effect, high open-circuit voltage, and durability. Supercapacitors, another key class of energy storage devices, stand out with rapid charge/discharge rates, high power density, and long cycle lifetimes. Their capacity surpasses conventional capacitors, and their faster discharge enables quick electric vehicle charging. Interestingly, halide perovskite materials, originally designed for solar cells, have proven effective in energy storage due to their excellent ion diffusion properties (e.g., an experimentally measured room-temperature ionic conductivity of 10^{-8} S cm^{-1} for MAPI[82]). While ion diffusion was initially considered detrimental to solar cell performance, it is advantageous for lithium batteries and supercapacitors, enhancing their efficiency in energy storage applications.[8−10]

In MAPI, ionic diffusion, which is sustained by the presence of intrinsic defects (e.g., vacancies), is substantial and increases rapidly with rising temperature in the high-T, orientationally disordered phase.[38] In this work, we simulated pristine MAPI systems (i.e., with no defects), thus purposely excluding ionic transport. Nevertheless, recent studies in the context of solid-state electrolytes have emphasized the significant role of the vibrating nondiffuse crystal matrix in ion migration.[40,41,83−86] In particular, the interplay between mobile atoms and the anharmonic lattice dynamics of the host framework may enhance superionicity.

In this study, the high anharmonicity of the orientationally disordered phase of MAPI has been evidenced by a large accumulation of low-frequency phonon lattice modes (Figures 2−3) and a substantial vibrational contribution to the total phase transition entropy change, which amounts to approximately 80% (Table 1). Potential proxies for identifying good ionic conductors among HOIPs may thus include the average phonon frequency, which should be as low as possible, along with the lattice heat capacity and vibrational entropy, which should be as high as possible.[41] Nonetheless, it remains to be determined how the cross-vibrational-orientational entropy change term, $\Delta S_{vib\text{-}ang}$, is affected by the presence of crystalline defects and superionicity in order to further elucidate the mechanisms of ionic transport in HOIPs. These, and other related, interesting questions will be analyzed in detail in future works.

4. CONCLUSIONS

A comprehensive analysis of the orientational disorder and molecular correlations in the archetypal hybrid organic−inorganic perovskite (HOIP) MAPI has been presented, relying on atomistic MD−NpT simulations and advanced entropy calculations. The main findings of our computational research are the following. Both in the low-T ordered and high-T disordered phases, there is dynamical orientational disorder associated with rigid MA^+ rotations around the molecular C−N axis. This previously overlooked orientational degree of freedom positively contributes to the total phase-transition entropy change, ΔS_t. The correlations between MA cations are substantial, especially in the low-T ordered phase, and have a sizable augmenting effect on ΔS_t. Conformational molecular changes, on the other hand, are relatively infrequent in both low-T ordered and high-T disordered phases and do not appreciably contribute to the phase-transition entropy change. Interestingly, the couplings between the vibrational and orientational degrees of freedom are strengthened in the high-T disordered phase and have a substantial decreasing effect on ΔS_t. Lastly, molecular correlations in the high-T disordered phase are predominant but markedly local; thus, the formation of nanoregions with a well-defined polarization is strongly suppressed. These fundamental outcomes may be tentatively generalized to other HOIP and have important ramifications for advanced energy and optoelectronic applications relying on this family of materials.

5. METHODS

5.1. MD Simulations. We used the LAMMPS simulation code[87] to perform systematic classical MD simulations in the NpT ensemble for bulk MAPI using the force field developed by Mattoni and coworkers.[37,38] The average temperature was set using a Nosé−Hoover thermostat with a mean fluctuation of 5 K. The simulation box contained 3072 atoms (equivalent to 256 MAPI unit cells), and periodic boundary conditions were applied along the three Cartesian directions. The long-range electrostatic interactions were calculated by using a particle−particle particle-mesh solver to compute Ewald sums up to an accuracy of 10^{-4} kcal mol^{-1} Å^{-1} in the atomic forces. The cutoff distance for the evaluation of the potential energy was set

https://doi.org/10.1021/acsami.4c12762
ACS Appl. Mater. Interfaces 2025, 17, 1428−1440

to 12 Å. To determine the phase-transition temperature of MAPI at zero pressure, we conducted comprehensive *NpT*-MD simulations in the temperature range $180 \leq T \leq 340$ K, taken at intervals of 10 K. In our MD−*NpT* simulations, the temperature steadily increased up to a targeted value of over 1 ns. Subsequently, the system was equilibrated at that selected temperature for 4 ns. The production runs then lasted for about 1 ns with $\Delta t = 0.5$ fs, from which the velocities of the atoms and other key quantities (e.g., the potential energy and volume of the system) were extracted. From the production MD−*NpT* runs, a total of 1000 equispaced configurations were retrieved to obtain uncorrelated structural data and generate accurate probability density functions (pdf).

5.2. Molecular Angular and Entropy Analysis. The MA^+ angular degrees of freedom have been retrieved from the atomic configurations generated during the MD−*NpT* simulations with the help of the freely available and open-source software ANGULA.[88] ANGULA is designed to automatically and unsupervisedly determine the angles defining the orientational structure of molecular disordered crystals from data files containing their atomic positions, both in the fixed "lab" and coMobile "rel" reference systems. Among its many capabilities, ANGULA can generate angular probability density maps and directional radial distribution functions directly from sequences of molecular configurations. In this study, the angular molecular entropy terms S_{ori}, $S_{ori\text{-}ori}$, and S_{conf} have been directly computed from the outputs of our MD−*NpT* simulations with ANGULA.[88]

AUTHOR INFORMATION

Corresponding Authors

Luis Carlos Pardo − *Group of Characterization of Materials, Departament de Física, Universitat Politècnica de Catalunya, Barcelona 08019, Spain; Research Center in Multiscale Science and Engineering, Universitat Politècnica de Catalunya, Barcelona 08019, Spain*; Email: luis.carlos.pardo@upc.edu

Claudio Cazorla − *Group of Characterization of Materials, Departament de Física, Universitat Politècnica de Catalunya, Barcelona 08019, Spain; Research Center in Multiscale Science and Engineering, Universitat Politècnica de Catalunya, Barcelona 08019, Spain*; orcid.org/0000-0002-6501-4513; Email: claudio.cazorla@upc.edu

Authors

Carlos Escorihuela-Sayalero − *Group of Characterization of Materials, Departament de Física, Universitat Politècnica de Catalunya, Barcelona 08019, Spain; Research Center in Multiscale Science and Engineering, Universitat Politècnica de Catalunya, Barcelona 08019, Spain*

Ares Sanuy − *Group of Characterization of Materials, Departament de Física, Universitat Politècnica de Catalunya, Barcelona 08019, Spain; Research Center in Multiscale Science and Engineering, Universitat Politècnica de Catalunya, Barcelona 08019, Spain*; orcid.org/0009-0000-5845-5241

Complete contact information is available at: https://pubs.acs.org/10.1021/acsami.4c12762

Notes

The authors declare no competing financial interest.

ACKNOWLEDGMENTS

C.C. acknowledges support from the Spanish Ministry of Science, Innovation and Universities under the fellowship RYC2018-024947-I and grants PID2020-112975GB-I00 and grant TED2021-130265B−C22. The authors also thankfully acknowledge technical support and computational resources at MareNostrum4 provided by the Barcelona Supercomputing Center (FI-2023-1-0002, FI-2023-2-0004, FI-2023-3-0004, FI-2024-1-0005, and FI-2024-2-0003). This work is part of the Maria de Maeztu Units of Excellence Programme CEX2023-001300 M funded by MCIN/AEI (10.13039/501100011033).

REFERENCES

(1) Hu, L.; Guan, X.; Wan, T.; Lin, C.-H.; Liu, S.; Zhu, R.; Chen, W.; Yao, Y.; Huang, C.-Y.; Yuan, L.; Shahrokhi, S.; Chu, D.; Cazorla, C.; Chen, J.; Yang, J.; Yi, J.; Huang, S.; Wu, T. Valence-regulated metal doping of mixed-halide perovskites to modulate phase segregation and solar cell performance. *ACS Energy Lett.* **2022**, *7*, 4150.

(2) Han, C.; Wang, Y.; Yuan, J.; Sun, J.; Zhang, X.; Cazorla, C.; Wu, X.; Wu, Z.; Shi, J.; Guo, J.; Huang, H.; Hu, L.; Liu, X.; Woo, H. Y.; Yuan, J.; Ma, W. Tailoring Phase Alignment and Interfaces via Polyelectrolyte Anchoring Enables Large-Area 2D Perovskite Solar Cells. *Angew. Chem., Int. Ed.* **2022**, *61*, No. e202205111.

(3) Guo, J.; Sun, J.; Hu, L.; Fang, S.; Ling, X.; Zhang, X.; Wang, Y.; Huang, H.; Han, C.; Zhou, Z.; Cazorla, C.; Yang, Y.; Chu, D.; Wu, T.; Yuan, J.; et al. Indigo: A Natural Molecular Passivator for Efficient Perovskite Solar Cells. *Adv. Energy Mater.* **2022**, *12*, 2200537.

(4) Wang, Y.; Duan, C.; Zhang, X.; Sun, J.; Ling, X.; Shi, J.; Hu, L.; Zhou, Z.; Wu, X.; Han, W.; Liu, X.; Cazorla, C.; Chu, D.; Huang, S.; Wu, T.; Yuan, J.; Ma, W. Electroluminiscent solar cells based on $CsPbI_3$ perovskites quantum dots. *Adv. Funct. Mater.* **2022**, *32*, 2108615.

(5) Choi, J.; Han, J. S.; Hong, K.; Kim, S. Y.; Jang, H. W. Organic-inorganic hybrid halide perovskites for memories, transistors, and artificial synapses. *Adv. Mater.* **2018**, *30*, 1704002.

(6) Kang, J.; Cho, J. H. Organic-inorganic hybrid perovskite electronics. *Phys. Chem. Chem. Phys.* **2020**, *22*, 13347.

(7) Liang, Y.; Li, F.; Zheng, R. Low-dimensional hybrid perovskites for field-effect transistors with improved stability: Progress and challenges. *Adv. Electron. Mater.* **2020**, *6*, 2000137.

(8) Zhang, W.; Eperon, G.; Snaith, H. Metal halide perovskites for energy applications. *Nat. Energy* **2016**, *1*, 16048.

(9) Zhang, L.; Miao, J.; Li, J.; Li, Q. Halide perovskite materials for energy storage applications. *Adv. Funct. Mater.* **2020**, *30*, 2003653.

(10) Han, B.; Zhao, J.; Luo, Z.; Cai, F.; Yuan, Z.; Zeng, H. Energy storage research of metal halide perovskites for rechargeable batteries. *Nano Energy* **2023**, *115*, 108646.

(11) Bermúdez-García, J. M.; Sánchez-Andújar, M.; Señarís-Rodríguez, M. A. A new playground for organic-inorganic hybrids: Barocaloric materials for pressure-induced solid-state cooling. *J. Phys. Chem. Lett.* **2017**, *8*, 4419.

(12) Bermúdez-García, J. M.; Sánchez-Andújar, M.; Castro-García, S.; López-Beceiro, J.; Artiaga, R.; Señarís-Rodríguez, M. A. Giant barocaloric effect in the ferroic organic-inorganic hybrid $[TPrA][Mn(dca)_3]$ perovskite under easily accessible pressures. *Nat. Commun.* **2017**, *8*, 15715.

(13) Li, J.; Barrio, M.; Dunstan, D. J.; Dixey, R.; Lou, X.; Tamarit, J.-Ll.; Phillips, A. E.; Lloveras, P. Colossal reversible barocaloric effects in layered hybrid perovskite $(C_{10}H_{21}NH_3)_2MnCl_4$ under low pressure near room temperature. *Adv. Funct. Mater.* **2021**, *31*, 2105154.

(14) Seo, J.; McGillicuddy, R. D.; Slavney, A. H.; Zhang, S.; Ukani, R.; Yakovenko, A. A.; Zheng, S.-L.; Mason, J. A. Colossal barocaloric effects with ultralow hysteresis in two-dimensional metal-halide perovskites. *Nat. Commun.* **2022**, *13*, 2536.

(15) Liu, Z.; Krückemeier, L.; Krogmeier, B.; Klingebiel, B.; Márquez, J. A.; Levcenko, S.; Öz, S.; Mathur, S.; Rau, U.; Unold, T.; Kirchartz, T. Open-circuit voltages exceeding 1.26 V in planar methylammonium lead iodide perovskite solar cells. *ACS Energy Lett.* **2019**, *4*, 110.

(16) Peng, W.; Wang, L.; Murali, B.; Ho, K.-T.; Bera, A.; Cho, N.; Kang, C.-F.; Burlakov, V. M.; Pan, J.; Sinatra, L.; Ma, C.; Xu, W.; Shi, D.; Alarousu, E.; Goriely, A.; He, J.-H.; Mohammed, O. F.; Wu, T.;

Bakr, O. M. Solution-grown monocrystalline hybrid perovskite films for hole-transporter-free solar cells. *Adv. Mater.* **2016**, *28*, 3383.
(17) Sheikh, A.; Bera, A.; Haque, M. A.; Rakhi, R. B.; Gobbo, S.; Alshareef, H. M.; Wu, T. Atmospheric effects on the photovoltaic performance of hybrid perovskite solar cells. *Sol. Energy Mater. Sol. Cells* **2015**, *137*, 6.
(18) Hu, L.; Duan, L.; Yao, Y.; Chen, W.; Zhou, Z.; Cazorla, C.; Lin, C.-H.; Guan, X.; Geng, X.; Wang, F.; Wan, T.; Wu, S.; Cheong, S.; Tilley, R. D.; Liu, S.; Yuan, J.; Chu, D.; Wu, T.; Huang, S. Quantum dot passivation of halide perovskite films with reduced defects, suppressed phase segregation, and enhanced stability. *Adv. Sci.* **2022**, *9*, 2102258.
(19) Zhao, C.; Cazorla, C.; Zhang, X.; Huang, H.; Zhao, X.; Li, D.; Shi, J.; Zhao, Q.; Ma, W.; Yuan, J. Fast organic cation exchange in colloidal perovskite quantum dots toward functional optoelectronic applications. *J. Am. Chem. Soc.* **2024**, *146*, 4913.
(20) Wasylishen, R.; Knop, O.; Macdonald, J. Cation rotation in methylammonium lead halides. *Solid State Commun.* **1985**, *56*, 581.
(21) Liu, S.; Guo, R.; Xie, F. The effects of organic cation rotation in hybrid organic-inorganic perovskites: A critical review. *Mater. Des.* **2022**, *221*, 110951.
(22) Lavén, R.; Koza, M. M.; Malavasi, L.; Perrichon, A.; Appel, M.; Karlsson, M. Rotational dynamics of organic cations in formamidinium lead iodide perovskites. *J. Phys. Chem. Lett.* **2023**, *14*, 2784.
(23) Gallop, N. P.; Selig, O.; Giubertoni, G.; Bakker, H. J.; Rezus, Y. L. A.; Frost, J.; Jansen, T. L. C.; Lovrincic, R.; Bakulin, A. A. Rotational cation dynamics in metal halide perovskites: Effect on phonons and material properties. *J. Phys. Chem. Lett.* **2018**, *9*, 5987.
(24) Fabini, D. H.; Siaw, T. A.; Stoumpos, C. C.; Laurita, G.; Olds, D.; Page, K.; Hu, J.; Kanatzidis, M.; Han, S.; Seshadri, R. Universal dynamics of molecular reorientation in hybrid lead iodide perovskites. *J. Am. Chem. Soc.* **2017**, *139*, 16875.
(25) Lahnsteiner, J.; Kresse, G.; Kumar, A.; Sarma, D. D.; Franchini, C.; Bokdam, M. Room-temperature dynamic correlation between methylammonium molecules in lead-iodine based perovskites: An *ab initio* molecular dynamics perspective. *Phys. Rev. B* **2016**, *94*, 214114.
(26) Frost, J. M.; Walsh, A. What is moving in hybrid halide perovskite solar cells? *Acc. Chem. Res.* **2016**, *49*, 528.
(27) Berruet, M.; Pérez-Martínez, J. C.; Romero, B.; Gonzales, C.; Al-Mayouf, A.; Guerrero, A.; Bisquert, J. Physical model for the current-voltage hysteresis and impedance of halide perovskite memristors. *ACS Energy Lett.* **2022**, *7*, 1214.
(28) Leguy, A. M.; Frost, J. M.; McMahon, A. P.; Sakai, V. G.; Kockelmann, W.; Law, C.; Li, X.; Foglia, F.; Walsh, A.; O'Regan, B. C.; Nelson, J.; Cabral, J. T.; Barnes, P. R. F. The dynamics of methylammonium ions in hybrid organic-inorganic perovskite solar cells. *Nat. Commun.* **2015**, *6*, 7124.
(29) Liu, S.; Cohen, R. E. Response of methylammonium lead iodide to external stimuli and caloric effects from molecular dynamics simulations. *J. Phys. Chem. C* **2016**, *120*, 17274.
(30) Escorihuela-Sayalero, C.; Pardo, L. C.; Romanini, M.; Obrecht, N.; Loehlé, S.; Lloveras, P.; Tamarit, J.-Ll.; Cazorla, C. Prediction and understanding of barocaloric effects in orientationally disordered materials from molecular dynamics simulations. *npj Comput. Mater.* **2024**, *10*, 13.
(31) Druzbicki, K.; Pinna, R. S.; Rudic, S.; Jura, M.; Gorini, G.; Fernandez-Alonso, F. Unexpected cation dynamics in the low-temperature phase of methylammonium lead iodide: The need for improved models. *J. Phys. Chem. Lett.* **2016**, *7*, 4701.
(32) Fabini, D. H.; Hogan, T.; Evans, H. A.; Stoumpos, C.; Kanatzidis, M. G.; Seshadri, R. Dielectric and thermodynamic signatures of low-temperature glassy dynamics in the hybrid perovskites $CH_3NH_3PbI_3$ and $HC(NH_2)_2PbI_3$. *J. Phys. Chem. Lett.* **2016**, *7*, 376−381.
(33) Shahrokhi, S.; Dubajic, M.; Dai, Z.-Z.; Bhattacharyya, S.; Mole, R. A.; Rule, K. C.; Bhadbhade, M.; Tian, R.; Mussakhanuly, N.; Guan, X.; Yin, Y.; Nielsen, M. P.; Hu, L.; Lin, C.-H.; Chang, S. L. Y.; Wang, D.; Kabakova, I. V.; Conibeer, G.; Bremner, S.; Li, X.-G.; Cazorla, C.; Wu, T. Anomalous structural evolution and glassy lattice in mixed-halide hybrid perovskites. *Small* **2022**, *18*, 2200847.
(34) Zhang, T.; Xu, K.; Li, J.; He, L.; Fu, D.-W.; Ye, Q.; Xiong, R.-G. Ferroelectric hybrid organic-inorganic perovskites and their structural and functional diversity. *Natl. Sci. Rev.* **2023**, *10*, nwac240.
(35) Fransson, E.; Rahm, J. M.; Wiktor, J.; Erhart, P. Revealing the free energy landscape of halide perovskites: Metastability and transition characters in $CsPbBr_3$ and $MAPbI_3$. *Chem. Mater.* **2023**, *35*, 8229.
(36) Shahrokhi, S.; Gao, W.; Wang, Y.; Anandan, P. R.; Rahaman, M. Z.; Singh, S.; Wang, D.; Cazorla, C.; Yuan, G.; Liu, J.-M.; Wu, T. Emergence of ferroelectricity in halide perovskites. *Small Methods* **2020**, *4*, 2000149.
(37) Mattoni, A.; Filippetti, A.; Saba, M. I.; Delugas, P. Methylammonium rotational dynamics in lead halide perovskite by classical molecular dynamics: The role of temperature. *J. Phys. Chem. C* **2015**, *119*, 17421−17428.
(38) Mattoni, A.; Filippetti, A.; Caddeo, C. Modeling hybrid perovskites by molecular dynamics. *J. Phys.: Condens. Matt.* **2017**, *29*, 043001.
(39) Kim, D.; Yun, J. S.; Sagotra, A.; Mattoni, A.; Sharma, P.; Kim, J.; Lee, D. S.; Lim, S.; O'Reilly, P.; Brinkman, L.; Green, M. A.; Huang, S.; Ho-Baillie, A.; Cazorla, C.; Seidel, J. Charge carrier transport properties of twin domains in halide perovskites. *J. Mater. Chem. A* **2023**, *11*, 16743.
(40) Sagotra, A. K.; Chu, D.; Cazorla, C. Influence of lattice dynamics on lithium-ion conductivity: A first-principles study. *Phys. Rev. Mater.* **2019**, *3*, 035405.
(41) López, C.; Emperador, A.; Saucedo, E.; Rurali, R.; Cazorla, C. Universal ion-transport descriptors and classes of inorganic solid-state electrolytes. *Mater. Horiz.* **2023**, *10*, 1757.
(42) Cazorla, C.; Boronat, J. Simulation and understanding of atomic and molecular quantum crystals. *Rev. Mod. Phys.* **2017**, *89*, 035003.
(43) Cover, T. M.; Thomas, J. A. *Elements of Information Theory (Wiley Series in Telecommunications and Signal Processing)*; Wiley-Interscience: USA, 2006.
(44) Pathria, R. *Statistical Mechanics*; Elsevier Science and Technology Books, 1972.
(45) Lazaridis, T.; Karplus, M. Orientational correlations and entropy in liquid water. *J. Chem. Phys.* **1996**, *105*, 4294.
(46) Henao, A.; Busch, S.; Guàrdia, E.; Tamarit, J. Ll.; Pardo, L. C. The structure of liquid water beyond the first hydration shell. *Phys. Chem. Chem. Phys.* **2016**, *18*, 19420.
(47) Pardo, L. C.; Henao, A.; Vispa, A. Characterizing ordering in liquids: An information theoretic approach. *J. Non-Cryst. Solids* **2015**, *407*, 220.
(48) Zeng, M.; Escorihuela-Sayalero, C.; Ikeshoji, T.; Takagi, S.; Kim, S.; Orimo, S.; Barrio, M.; Tamarit, J.-Ll.; Lloveras, P.; Cazorla, C.; Sau, K. Colossal reversible barocaloric effects in a plastic crystal mediated by lattice vibrations and ion diffusion. *Adv. Sci.* **2024**, *11*, 2306488.
(49) Sanuy, A.; Escorihuela-Sayalero, C.; Pardo, L. C.; Cazorla, C. *Molecular Origins of Colossal Barocaloric Effects in Plastic Crystals*, 2024.
(50) Cazorla, C.; Alfè, D.; Gillan, M. J. Constraints on the phase diagram of molybdenum from first-principles free-energy calculations. *Phys. Rev. B* **2012**, *85*, 064113.
(51) Cazorla, C.; Alfè, D.; Gillan, M. J. Melting properties of a simple tight-binding model of transition metals: I.The region of half-filled *d*-band. *J. Chem. Phys.* **2009**, *130*, 174707.
(52) Brivio, F.; Frost, J. M.; Skelton, J. M.; Jackson, A. J.; Weber, O. J.; Weller, M. T.; Goñi, A. R.; Leguy, A. M. A.; Barnes, P.; Walsh, A. Lattice dynamics and vibrational spectra of the orthorhombic, tetragonal, and cubic phases of methylammonium lead iodide. *Phys. Rev. B* **2015**, *92*, 144308.
(53) Cazorla, C. Refrigeration based on plastic crystals. *Nature* **2019**, *567*, 470.

https://doi.org/10.1021/acsami.4c12762
ACS Appl. Mater. Interfaces 2025, 17, 1428−1440

(54) Sau, K.; Ikeshoji, T.; Takagi, S.; Orimo, S.; Errandonea, D.; Chu, D.; Cazorla, C. Colossal barocaloric effects in the complex hydride $Li_2B_{12}H_{12}$. *Sci. Rep.* **2021**, *11*, 11915.
(55) Lloveras, P.; Aznar, A.; Barrio, M.; Negrier, Ph.; Popescu, C.; Planes, A.; Mañosa, L.; Stern-Taulats, E.; Avramenko, A.; Mathur, N. D.; Moya, X.; Tamarit, J.-Ll. Colossal barocaloric effects near room temperature in plastic crystals of neopentylglycol. *Nat. Commun.* **2019**, *10*, 1803.
(56) Salvatori, A.; Aguilà, D.; Aromí, G.; Mañosa, L.; Planes, A.; Lloveras, P.; Pardo, L. C.; Appel, M.; Nataf, G. F.; Giovannelli, F.; Barrio, M.; Tamarit, J.-Ll.; Romanini, M. Large barocaloric effects in two novel ferroelectric molecular plastic crystals. *J. Mater. Chem. A* **2023**, *11*, 12140−12150.
(57) Pérez-Osorio, M. A.; Milot, R. L.; Filip, M. R.; Patel, J. B.; Herz, L. M.; Johnston, M. B.; Giustino, F. Vibrational properties of the organic-inorganic halide perovskite $CH_3NH_3PbI_3$ from theory and experiment: Factor group analysis, first-principles calculations, and low-temperature infrared spectra. *J. Phys. Chem. C* **2015**, *119*, 25703.
(58) Mattoni, A.; Filippetti, A.; Saba, M. I.; Caddeo, C.; Delugas, P. Temperature evolution of methylammonium trihalide vibrations at the atomic scale. *J. Phys. Chem. Lett.* **2016**, *7*, 529−535.
(59) Romanini, M.; Negrier, P.; Tamarit, J.-Ll.; Capaccioli, S.; Barrio, M.; Pardo, L. C.; Mondieig, D. Emergence of glassy-like dynamics in an orientationally ordered phase. *Phys. Rev. B* **2012**, *85*, 134201.
(60) Gebbia, J. F.; Ramos, M. A.; Szewczyk, D.; Jezowski, A.; Krivchikov, A. I.; Horbatenko, Y. V.; Guidi, T.; Bermejo, F. J.; Tamarit, J.-Ll. Glassy anomalies in the low-temperature thermal properties of a minimally disordered crystalline solid. *Phys. Rev. Lett.* **2017**, *119*, 215506.
(61) Moratalla, M.; Gebbia, J. F.; Ramos, M. A.; Pardo, L. C.; Mukhopadhyay, S.; Rudić, S.; Fernandez-Alonso, F.; Bermejo, F. J.; Tamarit, J.-Ll. Emergence of glassy features in halomethane crystals. *Phys. Rev. B* **2019**, *99*, 024301.
(62) Zuriaga, M.; Pardo, L. C.; Lunkenheimer, P.; Tamarit, J.-Ll.; Veglio, N.; Barrio, M.; Bermejo, F. J.; Loidl, A. New microscopic mechanism for secondary relaxation in glasses. *Phys. Rev. Lett.* **2009**, *103*, 075701.
(63) Chen, T.; Foley, B. J.; Ipek, B.; Tyagi, M.; Copley, J. R. D.; Brown, C. M.; Choi, J. J.; Lee, S. H. Rotational dynamics of organic cations in the $CH_3NH_3PbI_3$ perovskite. *Phys. Chem. Chem. Phys.* **2015**, *17*, 31278−31286.
(64) Gebbia, J. F.; Aristizabal, A. H.; Negrier, P.; Aguilà, D.; Tamarit, J.-Ll.; Pardo, L. C. Dynamics and local ordering of pentachloronitrobenzene: a molecular-dynamics investigation. *Phys. Chem. Chem. Phys.* **2023**, *25*, 30553.
(65) Cazorla, C. Novel mechanocaloric materials for solidstate cooling applications. *Appl. Phys. Rev.* **2019**, *6*, 041316.
(66) Lloveras, P.; Tamarit, J.-Ll. Advances and obstacles in pressure-driven solid-state cooling: A review of barocaloric materials. *MRS Energy Sustain.* **2021**, *8*, 3.
(67) Rurali, R.; Escorihuela-Sayalero, C.; Tamarit, J.-Ll.; Íñiguez-González, J.; Cazorla, C. Giant photocaloric effects across a vast temperature range in ferroelectric perovskites. *Phys. Rev. Lett.* **2024**, *133*, 116401.
(68) Ren, L.; Wang, Y.; Wang, M.; Wang, S.; Zhao, Y.; Cazorla, C.; Chen, C.; Wu, T.; Jin, K. Tuning magnetism and photocurrent in Mn-doped organic-inorganic perovskites. *J. Phys. Chem. Lett.* **2020**, *11*, 2577.
(69) Krishnamurthy, S.; Pandey, P.; Kaur, J.; Chakraborty, S.; Nayak, P. K.; Sadhanala, A.; Ogale, S. Organic-inorganic hybrid and inorganic halide perovskites: structural and chemical engineering, interfaces and optoelectronic properties. *J. Phys. D: Appl. Phys.* **2021**, *54*, 133002.
(70) Zhu, L.; Wei, Z.; Yi, Y. Exciton binding energies in organic photovoltaic materials: A theoretical perspective. *J. Phys. Chem. C* **2022**, *126*, 14.
(71) Liu, C.; Errea, I.; Ding, C.; Pickard, C.; Conway, L. J.; Monserrat, B.; Fang, Y. W.; Lu, Q.; Sun, J.; Boronat, J.; et al. Excitonic insulator to superconductor phase transition in ultra-compressed helium. *Nat. Commun.* **2023**, *14*, 4458.
(72) Wright, A. D.; Verdi, C.; Milot, R. L.; Eperon, G. E.; Pérez-Osorio, M. A.; Snaith, H. J.; Giustino, F.; Johnston, M. B.; Herz, L. M. Electron-phonon coupling in hybrid lead halide perovskites. *Nat. Commun.* **2016**, *7*, 11755.
(73) Lin, Q.; Armin, A.; Nagiri, R. C. R.; Burn, P. L.; Meredith, P. Electro-optics of perovskite solar cells. *Nat. Photonics* **2015**, *9*, 106.
(74) Frost, J. M.; Butler, K. T.; Walsh, A. Molecular ferroelectric contributions to anomalous hysteresis in hybrid perovskite solar cells. *APL Mater.* **2014**, *2*, 081506.
(75) Quarti, C.; Mosconi, E.; De Angelis, F. Structural and electronic properties of organo-halide hybrid perovskites from ab initio molecular dynamics. *Phys. Chem. Chem. Phys.* **2015**, *17*, 9394.
(76) Grancini, G.; Srimath Kandada, A. R.; Frost, J. M.; Barker, A. J.; De Bastiani, M.; Gandini, M.; Marras, S.; Lanzani, G.; Walsh, A.; Petrozza, A. Role of microstructure in the electron-hole interaction of hybrid lead halide perovskites. *Nat. Photonics* **2015**, *9*, 695.
(77) Zhao, X.; Vanderbilt, D. Phonons and lattice dielectric properties of zirconia. *Phys. Rev. B* **2002**, *65*, 075105.
(78) Leite Alves, H. W.; Neto, A. R. R.; Scolfaro, L. M. R.; Myers, T. H.; Borges, P. D. Lattice contribution to the high dielectric constant of PbTe. *Phys. Rev. B* **2013**, *87*, 115204.
(79) Cochran, W.; Cowley, R. A. Dielectric constants and lattice vibrations. *J. Phys. Chem. Solids* **1962**, *23*, 447.
(80) Brivio, F.; Butler, K. T.; Walsh, A.; van Schilfgaarde, M. Relativistic quasiparticle self-consistent electronic structure of hybrid halide perovskite photovoltaic absorbers. *Phys. Rev. B* **2014**, *89*, 155204.
(81) Miyata, A.; Mitioglu, A.; Plochocka, P.; Portugall, O.; Wang, J. T.; Stranks, S. D.; Snaith, H. J.; Nicholas, R. J. Direct measurement of the exciton binding energy and effective masses for charge carriers in organic-inorganic tri-halide perovskites. *Nat. Phys.* **2015**, *11*, 582.
(82) Zhang, H.; Lin, H.; Liang, C.; Liu, H.; Liang, J.; Zhao, Y.; Zhang, W.; Sun, M.; Xiao, W.; Li, H.; Polizzi, S.; Li, D.; Zhang, F.; He, Z.; Choy, W. C. H. Organic-inorganic perovskite light-emitting electrochemical cells with a large capacitance. *Adv. Funct. Mater.* **2015**, *25*, 7226.
(83) Ren, Q.; Gupta, M. K.; Jin, M.; Ding, J.; Wu, J.; Chen, Z.; Lin, S.; Fabelo, O.; Rodríguez-Velamazán, J. A.; Kofu, M.; Nakajima, K.; Wolf, M.; Zhu, F.; Wang, J.; Cheng, Z.; Wang, G.; Tong, X.; Pei, Y.; Delaire, O.; Ma, J. Extreme phonon anharmonicity underpins superionic diffusion and ultralow thermal conductivity in argyrodite Ag_8SnSe_6. *Nat. Mater.* **2023**, *22*, 999.
(84) Gupta, M. K.; Ding, J.; Bansal, D.; Abernathy, D. L.; Ehlers, G.; Osti, N. C.; Zeier, W. G.; Delaire, O. Strongly anharmonic phonons and their role in superionic diffusion and ultralow thermal conductivity of Cu_7PSe_6. *Adv. Energy Mater.* **2022**, *12*, 2200596.
(85) Muy, S.; Schlem, R.; Shao-Horn, Y.; Zeier, W. G. Phonon-ion interactions: Designing ion mobility based on lattice dynamics. *Adv. Energy Mater.* **2021**, *11*, 2002787.
(86) Gupta, M. K.; Ding, J.; Osti, N. C.; Abernathy, D. L.; Arnold, W.; Wang, H.; Hood, Z.; Delaire, O. Fast Na diffusion and anharmonic phonon dynamics in superionic Na_3PS_4. *Energy Environ. Sci.* **2021**, *14*, 6554.
(87) Plimpton, S. Fast parallel algorithms for short-range molecular dynamics. *J. Comput. Phys.* **1995**, *117*, 1.
(88) https://gcm.upc.edu/en/members/luis-carlos/angula/ANGULA, (2024).

https://doi.org/10.1021/acsami.4c12762
ACS Appl. Mater. Interfaces 2025, 17, 1428−1440